



# Selectively located Pt clusters on Au/CeO<sub>2</sub> for highly robust water-gas shift reaction via atomic layer deposition

Yuanting Tang<sup>a,1</sup>, Zhang Liu<sup>a,1</sup>, Rongli Ye<sup>b</sup>, Rui Zhao<sup>a</sup>, Yaohui Dun<sup>a</sup>, Yunkun Zhao<sup>c</sup>,  
Xiao Liu<sup>b,\*</sup>, Rong Chen<sup>b</sup>, Bin Shan<sup>a,\*</sup>

<sup>a</sup> State Key Laboratory of Materials Processing and Die and Mould Technology and School of Materials Science and Engineering, Huazhong University of Science and Technology, Wuhan, Hubei 430074, People's Republic of China

<sup>b</sup> State Key Laboratory of Intelligent Manufacturing Equipment and Technology and School of Mechanical Science and Engineering, Huazhong University of Science and Technology, Wuhan, Hubei 430074, People's Republic of China

<sup>c</sup> State Key Laboratory of Advanced Technologies for Comprehensive Utilization of Platinum Metals, Kunming Institute of Precious Metals, Kunming 650106, People's Republic of China

## ARTICLE INFO

### Keywords:

Water gas shift reaction  
Au catalysts  
Selective atomic layer deposition  
Pt sub-nanoclusters  
Anti-poisoning

## ABSTRACT

Au catalysts have shown outstanding low temperature catalytic activity toward water-gas shift (WGS) reaction, but they are struggling with the durability concerns. Herein, Pt clusters are selectively located on Au/CeO<sub>2</sub> through atomic layer deposition method to activate the interfacial active sites poisoned by intermediate species. The selective method effectively avoids the coverage of Au surface sites by Pt atoms and maintains the low temperature catalytic activity of Au/CeO<sub>2</sub> catalyst. Durability test indicates that the Pt-activated Au/CeO<sub>2</sub> catalyst shows superior durability in WGS atmosphere (200 °C), which only attenuates 7.9% (from 78.0% to 70.1%) after 150 h. The analysis of surface intermediates and density functional theory calculations reveal that the introduction of Pt ensures the regenerative capacity of Au/CeO<sub>2</sub> active sites by facilitating the decomposition of intermediate species and the desorption of CO<sub>2</sub>.

## 1. Introduction

Currently, more than 80% of hydrogen supply is derived from the reforming of fossil fuels, containing 1% to 10% CO impurities, which must be removed to prevent their adverse effects on fuel cell electrodes [1–4]. This has brought considerable attention to water-gas shift (WGS) reaction that is not only a crucial process for the removal of CO and hydrogen purification, but also favourable for low operating temperatures due to exothermic nature [5,6]. Among various WGS catalysts, Au catalysts have exhibited outstanding low-temperature WGS activity, attributed to the essential role of Au/support active sites [7–9]. Unfortunately, these active sites are prone to be poisoned by reaction intermediates, such as carbonate and formate species, leading to a rapid activity decline, which limits the practical application of Au catalysts [10–12].

Extensive research has been conducted regarding the poisoning of Au catalysts, and it has been demonstrated that the poisoning effect of intermediate species is jointly determined by Au nanoparticles and the

nature of their supports [13–15]. Oxidized Au (Au<sup>3+</sup>) has been reported to promote the formation of surface intermediate (formate) species on Au/CeO<sub>2</sub> catalysts [16], while metallic Au (Au<sup>0</sup>) is more active in the decomposition of these intermediate species [17]. The size of Au nanoparticles has also been reported to affect the decomposition of surface intermediate species. The relationship between the size of Au nanoparticles and the reaction pathways of CO oxidation is investigated, which reveals that Au catalyst with larger particle size can intrinsic the decomposition reactivity of intermediate species [18]. In addition to Au, the adsorption strength and decomposition reactivity of intermediate species can also be affected by the nature of the supports [19–21]. One of the strategies to enhance the anti-poisoning ability of Au is to promote the decomposition of surface intermediate species by tuning the properties of surface oxygen species. By introducing elements such as Mn and Co into the oxide supports, the migration ability and reaction activity of surface oxygen vacancies can be enhanced, which further promotes the decomposition and desorption of surface intermediate species to varying degrees [22,23]. Another strategy to enhance the anti-poisoning of Au

\* Corresponding authors.

E-mail addresses: [xiaoliu@hust.edu.cn](mailto:xiaoliu@hust.edu.cn) (X. Liu), [bshan@mail.hust.edu.cn](mailto:bshan@mail.hust.edu.cn) (B. Shan).

<sup>1</sup> These authors contributed equally: Yuanting Tang, Zhang Liu

catalysts is to weaken the adsorption and generation of carbonate species on the active sites. For instance, it has been reported that the poisoning effect of intermediate species on Au catalyst is strongly depend on the its surface acidity/basicity. The incorporation of Zr and Fe into CeO<sub>2</sub> can enhance its acidity [24,25], which attenuates the adsorption of CO on the Au/CeO<sub>2</sub> active sites and reduces the accumulation of intermediate species. Nevertheless, this also result in a weakening of interfacial interactions, which is not expected. Although surface modification with In<sub>2</sub>O<sub>3</sub> has also been reported to induce the surface reconstruction to decrease the adsorption strength of CO, these coating methods could lead to the coverage of surface active sites [26,27]. Overall, the existing methods such as doping, surface modification, and coating can enhance the anti-poisoning ability of Au catalysts to varying degrees, but they can also inevitably lead to issues like weakening of interfacial interactions or coverage of surface active sites. It remains a grand challenge to develop an Au catalyst with excellent anti-poisoning ability while preserving its original active sites. The development of precise design and preparation strategy of Au catalyst for WGS reaction is necessary.

Unlike the poisoning phenomena observed on the surface of Au catalysts, Pt catalysts have been reported to exhibit promotional effects on the decomposition of carbonate and formate species [28–30]. However, Pt suffers from CO poisoning at low temperatures, which leads to a limited WGS activity [31]. Incorporating Pt into Au catalyst system, combined the high WGS activity of Au and the promotion effect of Pt on the decomposition of intermediate species, may yield surprisingly positive results. Herein, we ingeniously locate Pt clusters onto an Au/CeO<sub>2</sub> catalyst via a selective atomic layer deposition (ALD) method with octadecanethiol (ODT) as blocking agent [32], which effectively avoids the coverage of Au surface sites by Pt atoms. It is demonstrated that the Pt-activated Au/CeO<sub>2</sub> catalyst exhibits good WGS activity (0.020 s<sup>-1</sup> at 200 °C) and superior WGS durability with CO conversion only decrease from 78.0% to 70.1% in a 150-h long time test. Both the experimental and theoretical results reveal that the selective location of Pt effectively promotes the decomposition of surface intermediate species and desorption of CO<sub>2</sub>, enhancing the regenerative capability of interfacial active sites.

## 2. Experimental section

### 2.1. Catalysts synthesis

CeO<sub>2</sub> nanorods were fabricated by a hydrothermal method. Specifically, 1.96 g Ce(NO<sub>3</sub>)<sub>3</sub>·6 H<sub>2</sub>O was dissolved in deionized H<sub>2</sub>O (40 ml), and 30 ml of NaOH solution with a concentration of 10.5 mol/L was added incrementally. The suspension was kept stirred for half an hour, followed by a hydrothermal reaction at 100 °C for 24 h. The suspension was cooled to ambient temperature and then subjected to centrifugation. The resulting powder was dried at 80 °C overnight and calcined at 500 °C. The as-prepared sample was denoted as CeR.

Au nanoparticles were loaded on the CeR by the deposition-precipitation (DP) method. Typically, 28.8 g (NH<sub>4</sub>)<sub>2</sub>CO<sub>3</sub> was dissolved into deionized water (270 ml), and 3 g CeR was dispersed to the above solution. Then, 0.29 g AuHCl<sub>4</sub>·4 H<sub>2</sub>O was dissolved into deionized water (30 ml), and the obtained AuHCl<sub>4</sub> solution was added to the above suspension drop by drop. After that, the suspension was stirred for 1 h. Subsequently, the suspended particles were centrifuged. After an overnight dry at 80 °C, the powder was calcined at 400 °C, and the resulting catalyst is labeled as Au/CeR.

Pt was introduced onto the as-prepared Au catalyst by a selective ALD method with ODT as a blocking agent. Typically, 1 g Au/CeR is dispersed into the ethanol solution of ODT (5 mmol/L), and the mixture was stirred at 30 °C for 30 min. The suspended particles were centrifuged and dried at 60 °C overnight. The obtained sample was labeled as ODT-Au/CeR. Trimethyl (methylcyclopentadienyl) platinum (MeCpPtMe<sub>3</sub>) was used as the precursor of Pt. Before Pt deposition, Pt precursor was

heated to 65 °C, and the reaction chamber was set to 150 °C. The pulse pressure of Pt precursor was set to 0.2 torr, and 100 s Pt pulse was implemented on ODT-Au/CeR. The obtained sample was denoted as Pt-ODT-Au/CeR. Then, ODT was removed by calcining Pt-ODT-Au/CeR at 450 °C in an air atmosphere, and the obtained catalyst was labeled as Pt+Au/CeR.

For comparison, 25 s Pt pulse and 200 s Pt pulse were implemented on ODT-Au/CeR. The obtained samples after removing the ODT were denoted as Pt+Au/CeR-25s and Pt+Au/CeR-200s. Moreover, Pt was deposited directly onto Au/CeR and CeR through ALD and incipient wetness impregnation (IWI) methods. In detail, 20 s and 100 s ALD pulses were implemented directly on Au/CeR and CeR, respectively, and the obtained catalysts were labeled as Pt@Au/CeR and Pt/CeR-100s. Pt was also deposited onto Au/CeR and CeR via IWI method, with theoretical Pt mass loading of 0.3 wt% and 1 wt%, and the resulting samples were labeled as Pt@Au/CeR-IWI and Pt/CeR-IWI, respectively.

### 2.2. Catalysts characterization

The Au mass loading was assessed using an inductively coupled plasma atomic emission spectrometer (ICP-OES, Optima 4300 DV). The morphologies of the catalysts were investigated by a transmission electron microscopy (FEI Tecnai G2 F30) and a spherical aberration corrected transmission electron microscope (Titan Cubed Themis G2 300). Raman spectra measurements were carried out on a Raman spectrometer (inVia Reflex, Renishaw). X-ray photoelectron spectroscopy (XPS) was carried out on an X-ray photoelectron spectrometer (AXIS-ULTRA DLD-600 W) to investigate the elemental oxidation states. Electron paramagnetic resonance (EPR) spectra were collected on a Bruker EMXplus-6/1 spectrometer under room temperature.

Infrared spectrometer (Thermo Scientific Nicolet iS50) and mass spectrometer (HIDEN HPR20) were used to investigate the relationship between the calcination temperature and the removal of ODT. Specially, Au/CeR was initially filled into a Harrick *in-situ* cell, and after purging with Ar for half an hour, background data were collected. Then, Au/CeR was replaced with ODT-Au/CeR, followed by purging with Ar for half an hour. Subsequently, Ar was switched to 1% CO/Ar, and the spectrum was collected and recorded after 10 min. After that, the gas was switched from 1% CO/Ar to 20% O<sub>2</sub>/N<sub>2</sub>, and the catalyst was heated to 50 °C, and kept purging for half an hour. Then the catalyst was purged by Ar for half an hour at 50 °C. After that, the spectrum was collected in 1% CO/Ar at room temperature. Following the procedures mentioned above, the spectra for the samples subjected to different calcination temperatures were collected continuously until reacting 450 °C with an interval of 50 °C. Moreover, the data of the temperature-dependent decomposition of ODT were recorded with mass spectrometer. ODT-Au/CeR was placed in a chemisorption analyser (Finetec 4100), and heated up to 450 °C (5 °C/min). The exhaust gas was introduced into mass spectrometer, and the signals of CO<sub>2</sub> and H<sub>2</sub>O were collected.

Temperature-programmed reduction (TPR) of H<sub>2</sub> was carried out on a chemisorption analyzer (AMI-300). 30 mg catalysts were pretreated at 300 °C for an hour in an Ar atmosphere. After cooling down to room temperature, the Ar flow was switched to 10% H<sub>2</sub>/Ar. After H<sub>2</sub> signal stabilized, the catalysts were heated to 600 °C, and the data was collected by a thermal conductivity detector (TCD).

Temperature-programmed decomposition (TPD) experiments were performed on a chemisorption analyser (Finetec 4100) in an air atmosphere to analyze the accumulation of intermediate species on the surface of catalysts during the WGS durability test. Specifically, after durability tests, N<sub>2</sub> was introduced to purge the remaining CO and H<sub>2</sub>O. After being cooled down to room temperature, N<sub>2</sub> was switched to 20% O<sub>2</sub>/N<sub>2</sub>, and the exhaust gas was detected by a mass spectrometer (HIDEN HPR20). After the signals stabilized, the catalysts were heated up to 450 °C, and the signal of CO<sub>2</sub> was collected.

CO<sub>2</sub> temperature-programmed desorption (CO<sub>2</sub>-TPD) was carried out on Altamira instruments 300 (AMI-300) chemisorption analyzer.

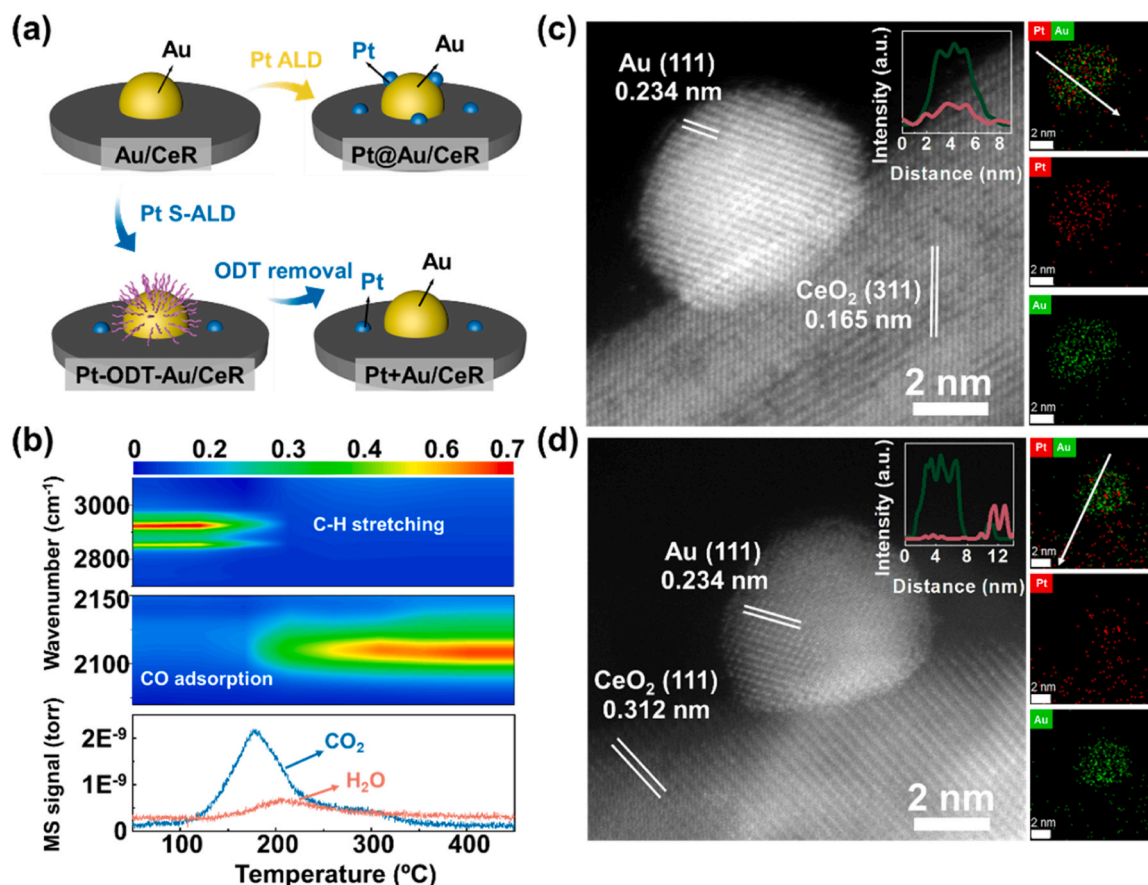


**Fig. 1.** Catalysts preparation processes and morphology characterizations. (a) Schematic diagram of the construction of Pt+Au/CeR and Pt@Au/CeR. (b) The MS signals (H<sub>2</sub>O and CO<sub>2</sub>) and DRIFTS results (collected in 1% CO/Ar atmosphere after cooling the sample to room temperature) of ODT-Au/CeR as a function of calcination temperature (in air atmosphere). HAADF-STEM images and EDS analysis of (c) Pt@Au/CeR and (d) Pt+Au/CeR.

30 mg catalysts were pretreated at 300 °C for half an hour in a He atmosphere. After the temperature decreased to room temperature, the gas flow was switched to CO<sub>2</sub>. After being treated in CO<sub>2</sub> for an hour, the CO<sub>2</sub> flow was switched to He. Once the signal from the thermal conductivity detector (TCD) stabilized, the catalysts were heated up to 600 °C.

*In situ* DRIFTS was carried out on a Thermo Scientific Nicolet iS50 infrared spectrometer. Samples were filled into a Harrick *in situ* cell, and being treated at 300 °C for 30 min with Ar. Afterward, the background spectrum was collected at room temperature. After that, 1% CO/Ar was introduced into the *in situ* cell, and the CO DRIFTS spectra were collected. For *in situ* DRIFTS in WGS atmosphere, the catalysts were cooled down to 50 °C after pretreatment, followed by switching the gas flow from Ar to 1% CO, 1% H<sub>2</sub>O/Ar. The catalysts were heated up to 200 °C and the spectra were collected every 50 °C. After collecting the *in situ* DRIFTS spectra of the catalysts, <sup>13</sup>CO isotope-labelling *in situ* DRIFTS experiment was performed at 200 °C to analyze the activity of surface intermediate species. The gas was switched from 1% CO, 1% H<sub>2</sub>O/Ar to 1% <sup>13</sup>CO, 1% H<sub>2</sub>O/Ar, and the spectra were collected over time.

### 2.3. Catalytic activity test

The catalytic activity and durability of the catalysts were evaluated on a chemisorption analyser (Finetec 4100). 100 mg of the catalysts were initially heated to 150 °C in a N<sub>2</sub> atmosphere. Then the N<sub>2</sub> flow was switched to 2% CO, 10% H<sub>2</sub>O/N<sub>2</sub> with a flow rate of 70 sccm. After stabilizing at 150 °C for half an hour, the catalysts were heated up to 300 °C, and the concentration of CO was collected by a gas analyzer (Horiba MEXA-584 L). The calculation method of CO conversion ( $X_{CO}$ ) is shown

below:

$$X_{CO} = 100 \times (1 - [CO]_{out}) / [CO]_{in}$$

where the CO concentrations in the outlet and inlet gas are given as  $[CO]_{out}$  and  $[CO]_{in}$ , respectively. For kinetic experiments, catalysts were mixed with quartz to ensure the conversion of CO below 20 %.

### 2.4. Computation methods

Density functional theory (DFT) calculations are conducted utilizing the Vienna Ab initio Simulation Package (VASP) [33,34]. The exchange-correlation energy is represented the generalized gradient approximation (GGA) employing the Perdew-Burke-Ernzerhof (PBE) functional [35]. The 3×4 supercell of CeO<sub>2</sub>(110) (15.76 Å×16.72 Å) with four atomic layers (144 atoms) is adopted in x-y plane to mitigate potential image interactions between loaded clusters. The Au/CeR and Pt+Au/CeR systems are simulated by a Au nanorod [36] and with a Pt<sub>5</sub> cluster supported on CeO<sub>2</sub>(110) surface. The bottom two layers are held in a fixed position to replicate the characteristics of the bulk environment, and the vacuum layer thickness is uniformly set to 15 Å across all slab models. To account for on-site Coulomb and exchange interactions, PBE+U method with a U-J value of 5.0 eV is applied to depict the Ce 4 f-orbital [37,38]. The Brillouin zones are discretized with gamma-centered Monkhorst-Pack k-meshes set at 1×1×1 considering the large size of surface cells. A Hellmann-Feynman force threshold of 0.05 eV/Å is employed to each relaxed atom, ensuring that the total energy changed by less than 10<sup>-5</sup> eV. The climbing image nudged elastic band (CI-NEB) is applied for identification the transition states (TS) associated with the dissociation of carbonate and formate. The



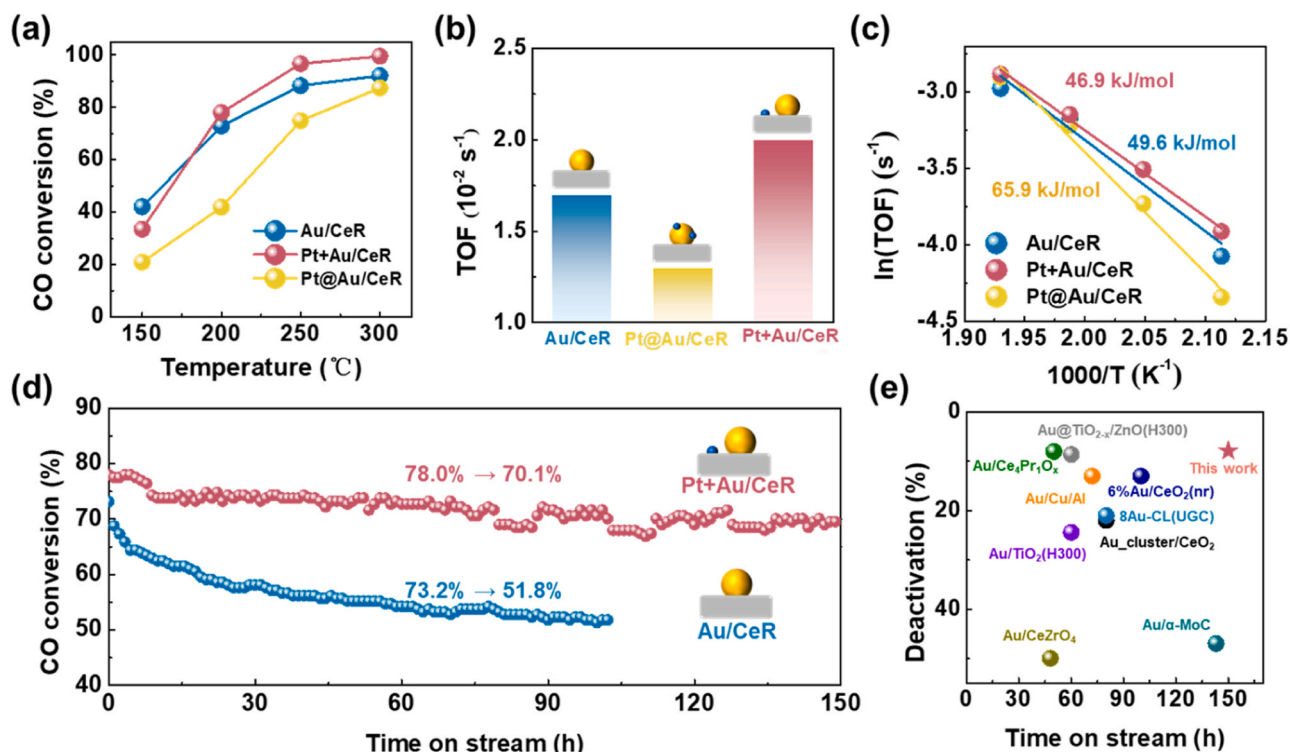


**Fig. 2.** Evaluation of activity and durability of the catalysts. (a) CO conversion of the catalysts as a function of reaction temperature. (b) Reaction rates (200 °C) and (c) apparent activation energies of the catalysts. (d) Results of durability tests. (e) Comparison of the WGS durability of the prepared Pt+Au/CeR with that of previously reported catalysts.

calculation of COHP (crystal orbital Hamiltonian population) for chemical bonding analysis is performed by the LOBSTER 4.0 package. The oxygen vacancy formation energy  $E_{O_v}$  and the adsorption energy  $E_{ad(X)}$  are defined as

$$E_{O_v} = E_{slab-O_v} + \frac{1}{2}E_{O_2} - E_{slab}$$

$$E_{ad(X)} = E_{slab+X} - (E_{slab} + E_X)$$

where  $E_{slab-O_v}$ ,  $E_{slab}$  and  $E_{O_2}$  are energies of the bare surface, O<sub>2</sub> molecule and the surface with an oxygen vacancy, respectively.  $E_X$  and  $E_{slab+X}$  correspond to energies of the adsorbates themselves and the surface with adsorbates, respectively.

### 3. Results and discussion

As shown in Fig. 1(a), Pt is introduced onto Au/CeO<sub>2</sub> through two different strategies, one of which is to selectively deposit Pt on the CeO<sub>2</sub> nanorod (CeR) support via an ALD method using ODT as blocking agent. The other strategy, as a comparison, is to deposit Pt directly onto the Au/CeR catalyst. The obtained catalysts are labeled as Pt+Au/CeR and Pt@Au/CeR, respectively. It is clear that the selective adsorption and removal of octadecanethiol (ODT) are crucial for the preparation of Pt+Au/CeR catalyst. The *in situ* diffuse reflectance infrared Fourier transform spectroscopy (DRIFTS) of ODT-Au/CeR (Fig. S1) shows obvious vibration peaks of C-H stretching (2958 cm<sup>-1</sup>, 2920 cm<sup>-1</sup> and 2850 cm<sup>-1</sup>), while these peaks are indistinct in the spectrum of ODT-CeR. Correspondingly, the CO chemisorption on Au vanishes after ODT adsorption (Fig. S2). These results suggest that ODT could selectively adsorb on the surface of Au rather than on the surface of CeR. These adsorbed ODT can be removed by calcinating in an air atmosphere at 450 °C. As illustrated in Fig. 1(b), as the calcination temperature increases, the intensity of C-H stretching vibration peaks (2958 cm<sup>-1</sup>, 2920 cm<sup>-1</sup> and 2850 cm<sup>-1</sup>) of ODT-Au/CeR gradually decreases and

disappears at around 200 °C. Correspondingly, the generation of CO<sub>2</sub> and H<sub>2</sub>O can be detected by the mass spectrometer (MS). As the calcination temperature further increasing, the chemical adsorption of CO on Au gradually enhances, indicating the removal of ODT and exposing the Au nanoparticles. These ODT are completely removed after the calcination temperature exceeding 400 °C, with no significant signals of CO<sub>2</sub> or H<sub>2</sub>O can be detected. The absence of the S 2p peak (163 eV) in the X-ray photoelectron spectroscopy (XPS) spectrum of Pt+Au/CeR further confirms the removal of ODT (Fig. S3).

Transmission electron microscopy (TEM) and aberration-corrected TEM are performed to visually characterize the morphologies of the catalysts. Statistical analysis (Fig. S4) indicates that the mean sizes in Au/CeR, Pt+Au/CeR and Pt@Au/CeR show no obvious difference, which is 4.2 nm ± 1.3 nm, 4.2 nm ± 1.2 nm, and 4.1 nm ± 1.0 nm, respectively. This is due to the fact the Pt mass loading in Pt@Au/CeR and Pt+Au/CeR are 0.32 wt% and 0.09 wt%, respectively, which are much lower than the mass loading of Au (2.16 wt%). As shown in Fig. 1 (c) and (d), facets like Au (111), CeO<sub>2</sub> (311) and CeO<sub>2</sub> (111) can be observed clearly in the HAADF-STEM images. Although it is challenging to distinguish Pt clusters from the HAADF-STEM images of Pt@Au/CeR and Pt+Au/CeR, Pt is prominently detected in both cases through EDS analysis, which is different from Au/CeR (Fig. S5). According to the EDS results, Pt in Pt@Au/CeR is distributed on both the Au and CeR support, and there is a higher Pt concentration on Au nanoparticle than that on CeR, owing to the easier nucleation of Pt on the metal surface [39–41]. This leads to a higher ratio of metallic Pt species in Pt@Au/CeR than that in Pt+Au/CeR, which is demonstrated by CO DRIFTS (Fig. S6) and the fitting analysis of Pt 4f (Fig. S7 and Table S1).[42] In comparison, Pt+Au/CeR shows a completely different spatial relationship between Pt clusters and Au nanoparticle. Most of Pt clusters in Pt+Au/CeR are distributed on the surface of CeR support rather than on the surface of Au nanoparticle due to the selective process.

The WGS activity and durability of the catalysts have been evaluated, and the results are shown in Fig. 2. It is demonstrated that Pt+Au/CeR

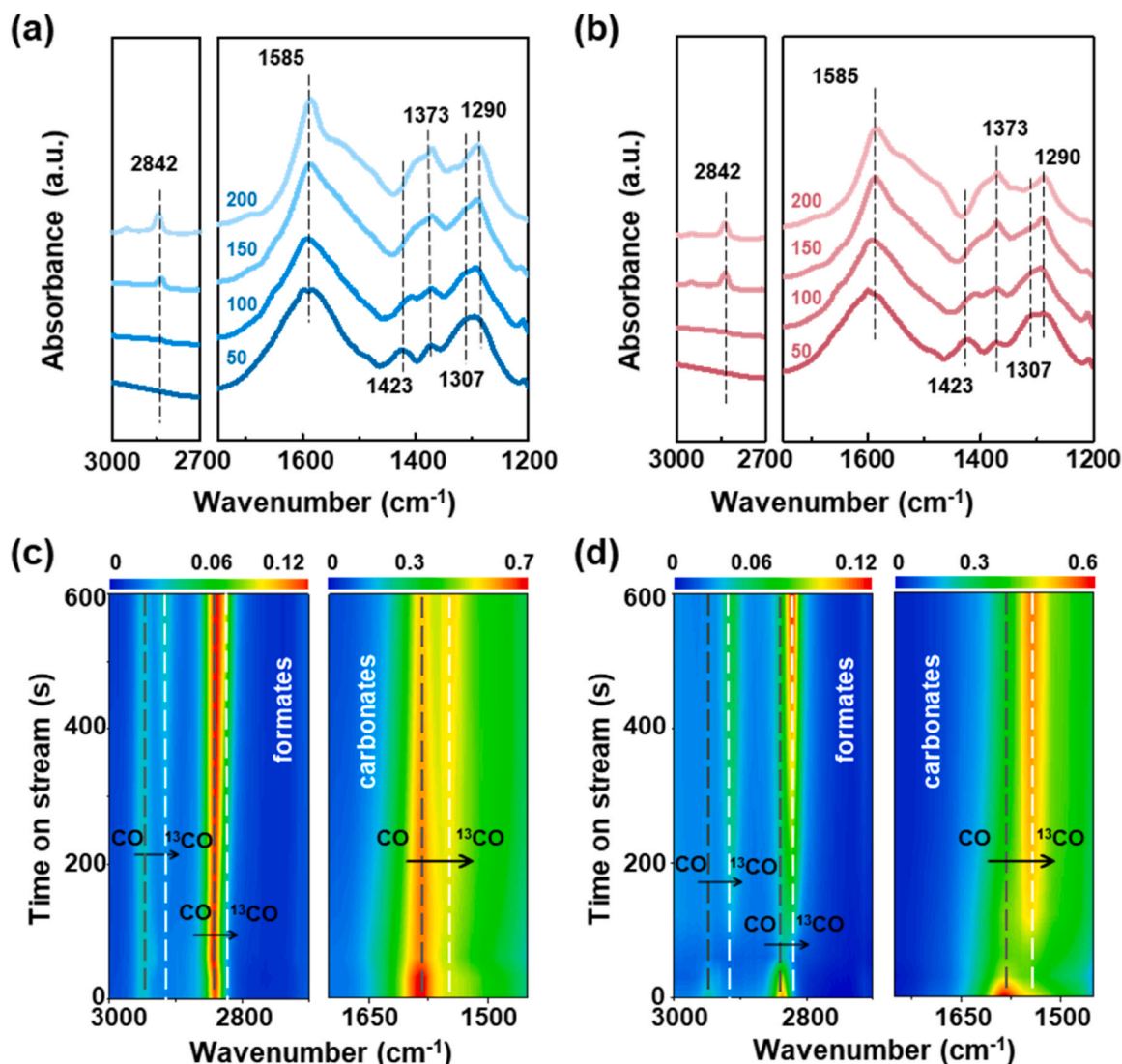


**Fig. 3.** Characterization of intermediate species on the catalysts. *In situ* DRIFTS results of (a) Au/CeR and (b) Pt+Au/CeR in the atmosphere of 1% CO, 1% H<sub>2</sub>O/Ar with the temperature range from 50 °C to 200 °C. Time-resolved *in situ* DRIFTS of (c) Au/CeR and (d) Pt+Au/CeR after switching 1% CO, 1% H<sub>2</sub>O/Ar to 1% <sup>13</sup>CO, 1% H<sub>2</sub>O/Ar at 200 °C.

exhibits good WGS activity, with a 78.0% CO conversion and a turnover frequency (TOF) of  $0.020 \text{ s}^{-1}$  at 200 °C, which is comparable to that of Au/CeR (CO conversion = 73.2%, TOF =  $0.017 \text{ s}^{-1}$ ) at low temperatures. In comparison, Pt@Au/CeR, which is obtained by directly depositing Pt onto the surface of Au/CeR, shows a much worse WGS performance, with a CO conversion of 41.9% at 200 °C. This is due to the fact that the direct depositing of Pt on Au/CeR leads to the coverage of a fraction of surface Au sites, and it is well known that Pt suffers from the issue of CO poisoning at low temperatures [43–45]. As the temperature increases, Pt+Au/CeR shows superior WGS activity compared to Au/CeR, and it achieves a conversion of 96.7% at 250 °C, which is higher than that of Au/CeR (88.3%). This improvement of WGS activity of Pt+Au/CeR is attributed to the increase of oxygen vacancies (Table S2) induced by the introduction of Pt clusters, [46–48] which is revealed by the analysis of surface oxygen species (Fig. S8 to Fig. S10). Further kinetics studies show that the apparent activation energy of Pt+Au/CeR (46.9 kJ/mol) is lower than that of Au/CeR (49.6 kJ/mol) and Pt@Au/CeR (65.9 kJ/mol). What's more, a series of control experiments are conducted via ALD and IWI methods, and the corresponding WGS performance of the obtained catalysts are presented in Fig. S11 and Fig. S12. Further durability test at 200 °C indicates that the

catalytic activity of Au/CeR significantly deteriorates under WGS conditions, and the corresponding CO conversion decreases from 73.2% to 51.8% after 100 h of testing. TEM tests (Fig. S13) show that the mean size of Au in Au/CeR, Pt@Au/CeR and Pt+Au/CeR after durability testing are  $4.5 \text{ nm} \pm 1.3 \text{ nm}$ ,  $4.6 \text{ nm} \pm 1.4 \text{ nm}$ , and  $4.6 \text{ nm} \pm 1.3 \text{ nm}$ , respectively, which exhibit no significant growth compared to the catalysts before durability tests. Regeneration experiment (Fig. S14) shows that this deactivation is almost completely reversible, indicating that poisoning of active sites is responsible for the deactivation of Au/CeR, which is consistent well with literature reports [49–51]. In comparison, Pt+Au/CeR exhibits excellent highly robust WGS durability, with the corresponding CO conversion only decreasing by 7.9% (from 78.0% to 70.1%) after 150 h of testing, which is superior compared to the WGS durability of Au catalysts reported in the literature (Fig. 2(e) and Table S3). Although Pt@Au/CeR also exhibits good stability (Fig. S15), as we mentioned above, its activity is much worse than that of Au/CeR. To compare the accumulation amount of intermediate species on the used Au/CeR and Pt+Au/CeR catalysts, temperature-programmed decomposition experiments (in air atmosphere) are implemented (Fig. S16). Both Au/CeR and Pt+Au/CeR exhibit MS signals corresponding to CO<sub>2</sub>, attributing to the decomposition of surface

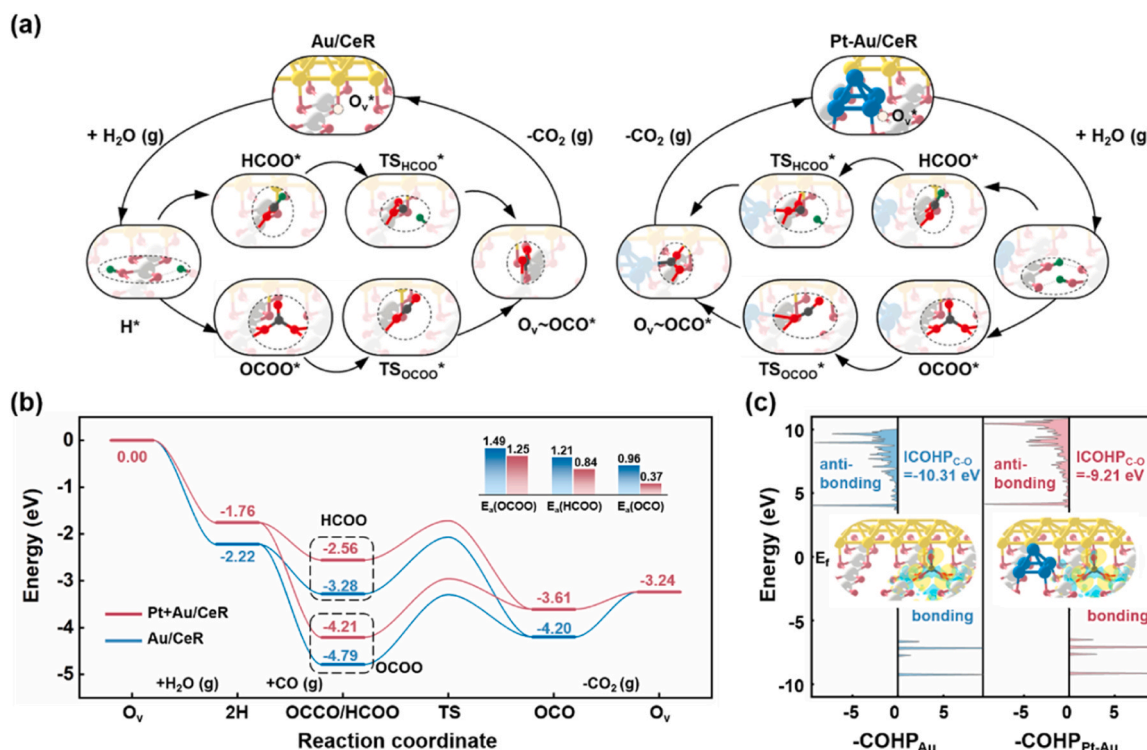


**Fig. 4.** Reaction pathways of intermediate species on Au/CeR and Pt+Au/CeR, and the corresponding DFT calculation results. (a) Schematic diagram and (b) energetic routes of carbonate and formate species pathways on Au/CeR and Pt+Au/CeR. (c) COHP localized on C-O bonds of  $\text{OCO}^*$  species and their charge density difference on Au/CeR and Pt+Au/CeR. The grey, blue, gold, black and green spheres represent Ce, Pt, Au, C and H atoms, respectively; the dark red and bright red spheres correspond to O atoms situated on  $\text{CeO}_2(110)$  slab and actively participating in the reaction. The yellow and cyan shadows in (c) represent positive and negative charges regions with  $0.0025 \text{ e bohr}^{-3}$  isosurface level.

intermediate species. For Pt+Au/CeR, there is no detectable  $\text{CO}_2$  signal after 200 °C. While, the signal of  $\text{CO}_2$  for Au/CeR can still be detected even at temperatures as high as 400 °C. The integration results show that the  $\text{CO}_2$  production from Au/CeR is three times more than that of Pt+Au/CeR.

*In situ* DRIFTS experiments are performed for further analysis of surface intermediate species. The obtained spectra of Au/CeR and Pt+Au/CeR in WGS atmosphere with temperatures ranging from 50 °C to 200 °C are shown in Fig. 3(a) and (b). At 50 °C, both Au/CeR and Pt+Au/CeR show four carbonate species adsorption peaks ( $1585 \text{ cm}^{-1}$ ,  $1423 \text{ cm}^{-1}$ ,  $1307 \text{ cm}^{-1}$  and  $1290 \text{ cm}^{-1}$ ), and a weak adsorption peak located at  $1373 \text{ cm}^{-1}$ , attributing to formate (or carbonate) species [52]. No obvious C-H stretching peaks can be detected in the range of  $2700 \text{ cm}^{-1}$  to  $3000 \text{ cm}^{-1}$ , indicating that there are few formate species on the surface of Au/CeR at 50 °C. As the temperature increases to above 150 °C, C-H stretching vibration peak ( $2842 \text{ cm}^{-1}$ ) has been observed both in the spectra of Au/CeR and Pt+Au/CeR, along with an enhancement of the peak located at  $1370 \text{ cm}^{-1}$ . This indicates that formate species are generated on the surface of Au/CeR and Pt+Au/CeR. Moreover, the *in situ* DRIFTS spectrum of Pt@Au/CeR is shown in Fig. S17 which shows no obvious difference to Au/CeR and Pt+Au/CeR. Due to the absence of notable disparities within the intermediate species, we further perform  $^{13}\text{C}$  isotope-labeling *in situ* DRIFTS experiments on the prepared catalysts at 200 °C to analyze the poisoning effect of the intermediates (carbonate and formate species) on Au/CeR and Pt+Au/CeR. Upon switching the gas from 1%  $\text{CO}$ , 1%  $\text{H}_2\text{O}/\text{Ar}$  to 1%  $^{13}\text{CO}$ , 1%  $\text{H}_2\text{O}/\text{Ar}$ , an obvious shift in the  $\text{CO}$  adsorption peaks over time can be observed for both Au/CeR and Pt+Au/CeR (Fig. S18). The peaks of carbonate species ( $1585 \text{ cm}^{-1}$ ) and formate species ( $2842 \text{ cm}^{-1}$ ) in the spectrum of Au/CeR (Fig. 3(c)) retain significant intensity after 10 min. In comparison, the peak of carbonate species in the spectrum of Pt+Au/CeR (Fig. 3(d)) rapidly shifts from  $1585 \text{ cm}^{-1}$  to  $1542 \text{ cm}^{-1}$ ,

These results indicate that carbonate species on the surface of Pt+Au/CeR are involved in a dynamic equilibrium reaction process, while these intermediate species on the surface of Au/CeR are poisoning species that are hard to be replaced. [53] In another word,

the surface of Pt+Au/CeR is less prone to be poisoned by carbonate species, which is consistent well with the  $\text{CO}_2$  temperature-programmed desorption ( $\text{CO}_2$ -TPD) results (Fig. S19). Additionally, the C-H stretching vibration in Pt+Au/CeR also shows a noticeable shift, which means that the introduction of Pt may not only avoid the poisoning of carbonate species on the active sites but also promote the participation of formate species in WGS reaction.

Density functional theory (DFT) calculations are employed to analyze how the Pt clusters affect the carbonate and formate species on Au/CeR. Pt+Au/CeR and Pt@Au/CeR catalysts are simulated by a Au nanorod and a  $\text{Pt}_5$  cluster supported on  $\text{CeO}_2(110)$  surface as depicted in Fig. S20 and Fig. S21 [54], [55]. The schematic diagram of the generation and decomposition of carbonate and formate species is shown in Fig. 4(a). In light of the oxygen vacancy formation energies ( $E_{\text{O}_v}$ ) in diverse coordination environments referring to Fig. S22, the interface comprising Au or Pt+Au clusters and  $\text{CeO}_2$  surface emerges as the most conducive sites for oxygen vacancy formation, which is considered as prime active site in catalytic process. With the adsorption and dissociation of  $\text{H}_2\text{O}$ , the vacancies are filled, providing active H atoms anchored at the adjacent surface oxygen atoms. The lower  $E_{\text{O}_v}$  in Pt+Au/CeR results in diminished exothermic  $\text{H}_2\text{O}$  dissociation. CO can directly adsorb at the interfacial sites to form carbonate ( $\text{OCO}^*$ ) species or attack H atoms from surface oxygen to form metastable formate ( $\text{HCOO}^*$ ) species, which have been observed by *in situ* DRIFTS mentioned above. These intermediate species further release an oxygen or hydrogen atom, leading to the formation of  $\text{OCO}$  species bound at the Ce-O-Au or Ce-Pt-Au sites. Finally, the  $\text{OCO}$  species desorb and produce  $\text{CO}_2$ . The higher CO adsorption energy and lower  $\text{OCO}^*$  decomposition



barrier (Fig. 4(b) and Fig. S23) on Pt+Au/CeR substantiate enhanced feasibility of carbonate conversion compared with Au/CeR. Further crystal orbital Hamilton population (COHP) analysis (Fig. 4(c)) indicates that Pt+Au/CeR exhibits more anti-bonding region and higher value of integrated COHP, which demonstrates the diminished OCOO binding strength on Pt+Au/CeR. Moreover, the specific Pt+Au/CeR interface structure induces a reduction of 0.37 eV in energy barrier for HCOO dissociation, attributed to enhanced dragging effect on OCO at Pt-Au interface as illustrated in Fig. S24. The subsequent desorption of OCO to form CO<sub>2</sub> involves an up-hill process of 0.96 eV on Au/CeR, but more readily on Pt+Au/CeR requiring only 0.37 eV (Fig. S25). To further quantitatively evaluate the activity of oxygen vacancy site on Au/CeR, Pt@Au/CeR and Pt+Au/CeR under experimentally relevant conditions, the state-to-state microkinetic model is employed according to catalytic cycle.[56] The reaction rates along carbonate and formate pathways of Au/CeR, Pt+Au/CeR and Pt@Au/CeR calculated by state-to-state microkinetic model are illustrated in Fig. S26 and Table S4. The OCOO pathway mainly contributes to activity in all cases compared to HCOO path. Within the considered temperature range of 400 K to 600 K, Pt+Au/CeR exhibits the highest activity, whereas Pt@Au/CeR demonstrates the lowest activity at lower temperatures, which aligns with our experimental findings. Based on the results mentioned above, the incorporation of Pt serves to effectively promote the regeneration of Au/CeR interfacial sites by attenuating the poisoning effects of intermediate species and facilitating the desorption of CO<sub>2</sub>.

#### 4. Conclusion

Pt activated Au/CeR catalyst is constructed via a selective ALD method with ODT as blocking agent, which effectively avoids the coverage of Au sites by Pt. The catalyst ensures the initial WGS activity of the as-prepared Pt+Au/CeR catalyst, which exhibits a comparable WGS activity to Au/CeR at low temperatures, and a better WGS activity at high temperatures. The introduction of Pt clusters enhances the renewability of active sites by promoting the decomposition of surface carbonate and formate species and further desorption of CO<sub>2</sub>. The CO conversion of Pt+Au/CeR only decreases from 78.0% to 70.1% in a 150-h long-time WGS durability test. Our work demonstrates the distinctive advantages of selective ALD in catalyst preparation, which can be extended to other systems.

#### CRedit authorship contribution statement

**Rongli Ye:** Investigation. **Xiao Liu:** Writing – review & editing, Visualization, Data curation. **Yunkun Zhao:** Writing – review & editing. **Yaohui Dun:** Investigation. **Rui Zhao:** Formal analysis. **Bin Shan:** Writing – review & editing, Visualization, Resources, Funding acquisition. **Rong Chen:** Resources, Project administration. **Zhang Liu:** Writing – original draft, Investigation. **Yuanting Tang:** Writing – original draft, Investigation, Formal analysis.

#### Declaration of Competing Interest

The authors declare that they have no known competing financial interests or personal relationships that could have appeared to influence the work reported in this paper.

#### Data Availability

Data will be made available on request.

#### Acknowledgments

This work was supported by the National Natural Science Foundation of China (Grants No. 52171209, 52271216, and 51835005), National Key R&D Program of China (2022YFF1500400), and the New

Cornerstone Science Foundation through the XPLOER PRIZE. We would also like to acknowledge the technical support from the Analytic Testing Center and Flexible Electronics Research Center of HUST.

#### Appendix A. Supporting information

Supplementary data associated with this article can be found in the online version.

#### Appendix A. Supporting information

Supplementary data associated with this article can be found in the online version at doi:10.1016/j.apcatb.2024.124218.

#### References

- [1] T. Hashimoto, T. Asada, S. Ogoshi, Y. Hoshimoto, Main group catalysis for H<sub>2</sub> purification based on liquid organic hydrogen carriers, *Sci. Adv.* 8 (2022) eade0189.
- [2] S.T. Wismann, J.S. Engbaek, S.B. Vendelbo, F.B. Bendixen, W.L. Eriksen, K. Aasberg-Petersen, C. Frandsen, I. Chorkendorff, P.M. Mortensen, Electrified methane reforming: a compact approach to greener industrial hydrogen production, *Science* 364 (2019) 756–759.
- [3] J.A. Rodriguez, S. Ma, P. Liu, J. Hrbek, J. Evans, M. Pérez, Activity of CeO<sub>x</sub> and TiO<sub>x</sub> nanoparticles grown on Au(111) in the water-gas shift reaction, *Science* 318 (2007) 1757–1760.
- [4] S.Y. Ahn, K.J. Kim, B.J. Kim, G.R. Hong, W.J. Jang, J.W. Bae, Y.K. Park, B.H. Jeon, H.S. Roh, From gray to blue hydrogen: trends and forecasts of catalysts and sorbents for unit process, *Renew. Sustain. Energy Rev.* 186 (2023) 113635.
- [5] X. Zhang, M.T. Zhang, Y.C. Deng, M.Q. Xu, L. Artiglia, W. Wen, R. Gao, B.B. Chen, S.Y. Yao, X.C. Zhang, M. Peng, J. Yan, A.W. Li, Z. Jiang, X.Y. Gao, S.F. Cao, C. Yang, A.J. Kropf, J.N. Shi, J.L. Xie, M.S. Bi, J.A. van Bokhoven, Y.W. Li, X.D. Wen, M. Flytzani-Stephanopoulos, C. Shi, W. Zhou, D. Ma, A stable low-temperature H<sub>2</sub>-production catalyst by crowding Pt on  $\alpha$ -MoC, *Nature* 589 (2021) 396–401.
- [6] J.Q. Zhao, Y. Bai, Z.H. Li, J.J. Liu, W. Wang, P. Wang, B. Yang, R. Shi, G.I. N. Waterhouse, X.D. Wen, Q. Dai, T.R. Zhang, Plasmonic Cu nanoparticles for the low-temperature photo-driven water-gas shift reaction, *Angew. Chem. Int. Ed.* 62 (2023) e202219299.
- [7] A. Mahdavi-Shakib, L.C. Rich, T.N. Whittaker, B.D. Chandler, Hydrogen adsorption at the Au/TiO<sub>2</sub> interface: quantitative determination and spectroscopic signature of the reactive interface hydroxyl groups at the active site, *ACS Catal.* 11 (2021) 15194–15202.
- [8] W. Grünert, D. Grossmann, H. Noei, M.M. Pohl, I. Sinev, A. De Toni, Y.M. Wang, M. Muhler, Low-temperature oxidation of carbon monoxide with Gold(III) ions supported on titanium oxide, *Angew. Chem. Int. Ed.* 53 (2014) 3245–3249.
- [9] J.C. Liu, L.L. Luo, H. Xiao, J.F. Zhu, Y. He, J. Li, Metal affinity of support dictates sintering of gold catalysts, *J. Am. Chem. Soc.* 144 (2022) 20601–20609.
- [10] C.E. Stere, J.A. Anderson, S. Chansai, J.J. Delgado, A. Goguet, W.G. Graham, C. Hardacre, S.F.R. Taylor, X. Tu, Z.Y. Wang, H. Yang, Non-thermal plasma activation of gold-based catalysts for low-temperature water-gas shift catalysis, *Angew. Chem. Int. Ed.* 56 (2017) 5579–5583.
- [11] Z. Boukha, J.R. González-velasco, M.A. Gutiérrez-Ortiz, Exceptional performance of gold supported on fluorinated hydroxyapatite catalysts in CO-cleanup of H<sub>2</sub>-rich stream: high activity and resistance under PEMFC operation conditions, *Appl. Catal. B-Environ.* 292 (2021) 120142.
- [12] J.J. Shi, H.L. Li, A. Genest, W.X. Zhao, P.F. Qi, T. Wang, G. Rupprechter, High-performance water gas shift induced by asymmetric oxygen vacancies: gold clusters supported by ceria-praseodymia mixed oxides, *Appl. Catal. B-Environ.* 301 (2022) 120789.
- [13] J. Saavedra, C.J. Pursell, B.D. Chandler, CO oxidation kinetics over Au/TiO<sub>2</sub> and Au/Al<sub>2</sub>O<sub>3</sub> catalysts: evidence for a common water-assisted mechanism, *J. Am. Chem. Soc.* 140 (2018) 3712–3723.
- [14] M. Sankar, Q. He, R.V. Engel, M.A. Sainna, A.J. Logsdail, A. Roldan, D.J. Willock, N. Agarwal, C.J. Kiely, G.J. Hutchings, Role of the support in gold-containing nanoparticles as heterogeneous catalysts, *Chem. Rev.* 120 (2020) 3890–3938.
- [15] H. Chen, L.J. Felling, H. Kersell, G. Yan, X. Zhao, J. Oliver-Meseguer, M. Jaugstetter, S. Nemsak, A. Hunt, I. Waluyo, H. Ogasawara, A.T. Bell, P. Sautet, M. Salmeron, Elucidating the active phases of CoO<sub>x</sub> films on Au(111) in the CO oxidation reaction, *Nat. Commun.* 14 (2023) 6889.
- [16] Y.B. Bu, Y.F. Chen, G.M. Jiang, X.M. Hou, S. Li, Z.T. Zhang, Understanding of Au-CeO<sub>2</sub> interface and its role in catalytic oxidation of formaldehyde, *Appl. Catal. B-Environ.* 260 (2020) 118138.
- [17] A. Karpenko, R. Leppelt, V. Plzak, R.J. Behm, The role of cationic Au<sup>3+</sup> and nonionic Au<sup>0</sup> species in the low-temperature water-gas shift reaction on Au/CeO<sub>2</sub> catalysts, *J. Catal.* 252 (2007) 231–242.
- [18] S.L. hen, F. Luo, Z.Q. Jiang, W.X. Huang, Size-dependent reaction pathways of low-temperature CO oxidation on Au/CeO<sub>2</sub> catalysts, *ACS Catal.* 5 (2015) 1653–1662.
- [19] M. Ziemba, J. Weyel, C. Hess, Elucidating the mechanism of the reverse water-gas shift reaction over Au/CeO<sub>2</sub> catalysts using operando and transient spectroscopies, *Appl. Catal. B-Environ.* 301 (2022) 120825.

- [20] T. Ishida, T. Murayama, A. Taketoshi, M. Haruta, Importance of size and contact structure of gold nanoparticles for the genesis of unique catalytic processes, *Chem. Rev.* 120 (2020) 464–525.
- [21] A.I.M. Rabee, D. Zhao, S. Cisneros, C.R. Kreyenschulte, V. Kondratenko, S. Bartling, C. Kubis, E.V. Kondratenko, A. Brückner, J. Rabeah, Role of interfacial oxygen vacancies in low-loaded Au-based catalysts for the low-temperature reverse water gas shift reaction, *Appl. Catal. B-Environ.* 321 (2023) 122083.
- [22] Z.D. Shen, E.R. Gao, X.Y. Meng, J.C. Xu, Y. Sun, J.L. Zhu, J. Li, Z.L. Wu, W. Wang, S.L. Yao, Q.G. Dai, Mechanistic insight into catalytic combustion of ethyl acetate on modified CeO<sub>2</sub> nanobelts: hydrolysis-oxidation process and shielding effect of acetates/alcoholates, *Environ. Sci. Technol.* 57 (2023) 3864–3874.
- [23] T. Tabakova, D. Dimitrov, M. Manzoli, F. Vindigni, P. Petrova, L. Ilieva, R. Zanella, K. Ivanov, Impact of metal doping on the activity of Au/CeO<sub>2</sub> catalysts for catalytic abatement of VOCs and CO in waste gases, *Catal. Commun.* 35 (2013) 51–58.
- [24] J.H. Carter, X. Liu, Q. He, S. Althabhan, E. Nowicka, S.J. Freakley, L.W. Niu, D. J. Morgan, Y.W. Li, J.W. Niemantsverdriet, S. Golunski, C.J. Kiely, G.J. Hutchings, Activation and deactivation of gold/ceria-zirconia in the low-temperature water-gas shift reaction, *Angew. Chem. Int. Ed.* 56 (2017) 16037–16041.
- [25] T.R. Reina, S. Ivanova, M.A. Centeno, J.A. Odriozola, The role of Au, Cu & CeO<sub>2</sub> and their interactions for an enhanced WGS performance, *Appl. Catal. B-Environ.* 187 (2016) 98–107.
- [26] X.M. Zhang, P.F. Tian, W.F. Tu, Z.Z. Zhang, J. Xu, Y.F. Han, Tuning the dynamic interfacial structure of copper-ceria catalysts by indium oxide during CO oxidation, *ACS Catal.* 8 (2018) 5261–5275.
- [27] J.J. Shi, A. Wittstock, C. Mahr, M.M. Murshed, T.M. Gesing, A. Rosenauer, M. Bäumer, Nanoporous gold functionalized with praseodymia-titania mixed oxides as a stable catalyst for the water-gas shift reaction, *Phys. Chem. Chem. Phys.* 21 (2019) 3278–3286.
- [28] M. Martinelli, J.D. Castro, N. Alhraki, M.E. Matamoros, A.J. Kropf, D.C. Cronauer, G. Jacobs, Effect of sodium loading on Pt/ZrO<sub>2</sub> during ethanol steam reforming, *Appl. Catal. A-Gen.* 610 (2021) 117947–117963.
- [29] Z. Hou, M. Chen, Y. Liu, J. Deng, L. Jing, R. Gao, W. Pei, Z. Li, H. Dai, Enhanced moisture resistance and catalytic stability of ethylene oxidation at room temperature by the ultrasmall MnO<sub>x</sub> cluster/Pt hetero-junction, *Appl. Catal. B-Environ.* 339 (2023) 123115–123126.
- [30] A. Gamal, K. Eid, A.M. Abdullah, Engineering of Pt-based nanostructures for efficient dry (CO<sub>2</sub>) reforming: strategy and mechanism for rich-hydrogen production, *Int. J. Hydrog. Energ.* 47 (2022) 5901–5928.
- [31] W. Chen, J. Cao, W. Fu, J. Zhang, G. Qian, J. Yang, D. Chen, X. Zhou, W. Yuan, X. Duan, Molecular-level insights into the notorious CO poisoning of platinum catalyst, *Angew. Chem. Int. Ed.* 61 (2022) e202200190.
- [32] X. Liu, Y. Su, R. Chen, Atomic-scale engineering of advanced catalytic and energy materials via atomic layer deposition for eco-friendly vehicles, *Int. J. Extrem. Manuf.* 5 (2023) 022005.
- [33] G. Kresse, D. Joubert, From ultrasoft pseudopotentials to the projector augmented-wave method, *Phys. Rev. B* 59 (1999) 1758–1775.
- [34] G. Kresse, J. Hafner, *Ab initio* molecular-dynamics simulation of the liquid-metal-amorphous-semiconductor transition in germanium, *Phys. Rev. B* 49 (1994) 14251–14269.
- [35] J.P. Perdew, K. Burke, M. Ernzerhof, Generalized gradient approximation made simple, *Phys. Rev. Lett.* 77 (1996) 3865–3868.
- [36] W. Song, E.J.M. Hensen, A computational DFT study of CO oxidation on a Au nanorod supported on CeO<sub>2</sub> (110): on the role of the support termination, *Catal. Sci. Technol.* 3 (2013) 3020.
- [37] V.I. Anisimov, J. Zaanen, O.K. Andersen, Band theory and Mott insulators: Hubbard *U* instead of Stoner *I*, *Phys. Rev. B* 44 (1991) 943–954.
- [38] M. Nolan, S.C. Parker, G.W. Watson, The electronic structure of oxygen vacancy defects at the low index surfaces of ceria, *Surf. Sci.* 595 (2005) 223–232.
- [39] X.R. Jiang, T.M. Gür, F.B. Prinz, S.F. Bent, Atomic layer deposition (ALD) co-deposited Pt-Ru binary and Pt skin catalysts for concentrated methanol oxidation, *Chem. Mater.* 22 (2010) 3024–3032.
- [40] D.Y. Chung, S. Park, H. Lee, H. Kim, Y.H. Chung, J.M. Yoo, D. Ahn, S.H. Yu, K. S. Lee, M. Ahmadi, H.X. Ju, H.D. Abruna, S.J. Yoo, B.S. Mun, Y.E. Sung, Activity-stability relationship in Au@Pt nanoparticles for electrocatalysis, *ACS Energy Lett.* 5 (2020) 2827–2834.
- [41] X.D. Du, Y. Lang, K. Cao, J.Q. Yang, J.M. Cai, B. Shan, R. Chen, Bifunctionally faceted Pt/Ru nanoparticles for preferential oxidation of CO in H<sub>2</sub>, *J. Catal.* 396 (2021) 148–156.
- [42] V. Pramhaas, M. Roiaz, N. Bosio, M. Corva, C. Rameshan, E. Vesselli, H. Grönbeck, G. Rupprechter, Interplay between CO disproportionation and oxidation: on the origin of the CO reaction onset on atomic layer deposition-grown Pt/ZrO<sub>2</sub> model catalysts, *ACS Catal.* 11 (2021) 208–214.
- [43] Q. Wang, Z.L. Zhao, M. Gu, CO gas induced phase separation in PtPb@Pt catalyst and formation of ultrathin Pb nanosheets probed by in situ transmission electron microscopy, *Small* 15 (2019) 1903122.
- [44] M. Yoo, Y.S. Yu, H. Ha, S. Lee, J.S. Choi, S. Oh, E. Kang, H. Choi, H. An, K.S. Lee, J. Y. Park, R. Celestre, M.A. Marcus, K. Nowrouzi, D. Taube, D.A. Shapiro, W. Jung, C. Kim, H.Y. Kim, A tailored oxide interface creates dense Pt single-atom catalysts with high catalytic activity, *Energy Environ. Sci.* 13 (2020) 1231–1239.
- [45] S.B. Xi, J. Zhang, K. Xie, Low-temperature water-gas shift reaction enhanced by oxygen vacancies in Pt-loaded porous single-crystalline oxide monoliths, *Angew. Chem.* 134 (2022) e202209851.
- [46] L. Song, X.B. Cao, L. Li, Engineering stable surface oxygen vacancies on ZrO<sub>2</sub> by hydrogen-etching technology: an efficient support of gold catalysts for water-gas shift reaction, *ACS Appl. Mater. Interfaces* 10 (2018) 31249–31259.
- [47] T. Tabakova, F. Boccuzzi, M. Manzoli, J.W. Sobczak, V. Idakiev, D. Andreeva, Effect of synthesis procedure on the low-temperature WGS activity of Au/Ceria catalysts, *Appl. Catal. B-Environ.* 49 (2004) 73–81.
- [48] R.S. Peng, S.J. Li, X.B. Sun, Q.M. Ren, L.M. Chen, M.L. Fu, J.L. Wu, D.Q. Ye, Size effect of Pt nanoparticles on the catalytic oxidation of toluene over Pt/CeO<sub>2</sub> catalysts, *Appl. Catal. B-Environ.* 220 (2018) 462–470.
- [49] X.Y. Liu, P.J. Guo, B. Wang, Z. Jiang, Y. Pei, K.N. Fan, M.H. Qiao, A comparative study of the deactivation mechanisms of the Au/CeO<sub>2</sub> catalyst for water-gas shift under steady-state and shutdown/start-up conditions in realistic reformate, *J. Catal.* 300 (2013) 152–162.
- [50] A.M. Abdel-Mageed, G. Kucerová, J. Bansmann, R.J. Behm, Active Au species during the low-temperature water gas shift reaction on Au/CeO<sub>2</sub>: a time-resolved operando XAS and DRIFTS study, *ACS Catal.* 7 (2017) 6471–6484.
- [51] A. Rezvani, A.M. Abdel-Mageed, T. Ishida, T. Murayama, M.P. Wojtan, R.J. Behm, CO<sub>2</sub> reduction to methanol on Au/CeO<sub>2</sub> catalysts: mechanistic insights from activation/deactivation and SSITKA measurements, *ACS Catal.* 10 (2020) 3580–3594.
- [52] Y. Denkwitz, A. Karpenko, V. Plzak, R. Leppelt, B. Schumacher, R.J. Behm, Influence of CO<sub>2</sub> and H<sub>2</sub> on the low-temperature water-gas shift reaction on Au/CeO<sub>2</sub> catalysts in idealized and realistic reformate, *J. Catal.* 246 (2007) 74–90.
- [53] T. Vergara, D. Gómez, B.L.D.O. Campos, K.H. Delgado, R. Gómez, A. Karelavic, Disclosing the reaction mechanism of CO<sub>2</sub> hydrogenation to methanol over CuCeO<sub>x</sub>/TiO<sub>2</sub>: a combined kinetic, spectroscopic, and isotopic study, *ACS Catal.* 13 (2023) 14699–14715.
- [54] I.X. Green, W.J. Tang, M. Neurock, J.T. Yates Jr, Spectroscopic observation of dual catalytic sites during oxidation of CO on a Au/TiO<sub>2</sub> catalyst, *Science* 333 (2011) 736–739.
- [55] X. Liu, S.F. Jia, M. Yang, Y.T. Tang, Y.W. Wen, S.Q. Chu, J.B. Wang, B. Shan, R. Chen, Activation of subnanometric Pt on Cu-modified CeO<sub>2</sub> via redox-coupled atomic layer deposition for CO oxidation, *Nat. Commun.* 11 (2020) 4240.
- [56] J. Yang, L. Shi, X. Liu, Y. Wen, K. Cho, Y. Zhao, R. Chen, B. Shan, Unravelling origins of Pd ensembles' activity in CO oxidation via state-to-state microkinetic analysis, *J. Catal.* 371 (2019) 276–286.